Catalysis Today xxx (xxxx) xxx–xxx

Contents lists available at ScienceDirect

Catalysis Today

journal homepage: www.elsevier.com/locate/cattod

Behaviour of Pt/TiO_2 catalysts with different morphological and structural characteristics in the photocatalytic conversion of ethanol aqueous solutions

Alberto C. Sola[a,b], Pilar Ramírez de la Piscina[a], Narcís Homs[a,b,*]

[a] Departament de Química Inorgànica i Orgànica, secció de Química Inorgànica, and Institut de Nanociència i Nanotecnologia, Universitat de Barcelona, Martí i Franquès 1-11, 08028, Barcelona, Spain

[b] Catalonia Institute for Energy Research (IREC), Jardins de les Dones de Negre 1, 08930, Barcelona, Spain

ARTICLE INFO

Keywords:
Pt/TiO_2photocatalysts
Renewable H_2
Photocatalytic C-C formation
Pt/anatase photocatalyst
2,3-Butanediol from ethanol

ABSTRACT

Pt/TiO_2 catalysts with a similar Pt dispersion and different morphological and structural characteristics were prepared, characterized and used in the photocatalytic transformation of aqueous ethanol solutions at room temperature. The characteristics of the catalysts allowed the comparison of their catalytic behaviour as a function their structural and morphological properties, which determined both the amount of hydrogen produced and the nature of the carbon-containing products. The characterization techniques used include N_2 physisorption, XRD, TEM, Raman, UV–vis and XP spectroscopies, H_2-TPR and CO chemisorption. Temperature programmed desorption of post-reaction catalysts was followed by DRIFTS-MS. The Pt/TiO_2 catalysts contained only anatase (Pt/A catalysts) or both anatase and rutile (Pt/AR catalysts), and had surface area from approximately 50 $m^2 \cdot g^{-1}$ to 100 $m^2 \cdot g^{-1}$ with mean pore sizes varying from 5 to 43 nm. Pt/TiO_2 catalysts having surface area of approximately 50 $m^2 \cdot g^{-1}$ and mean pore size of 30–40 nm produced more H_2 than the other catalysts, with Pt/A50 being the catalyst which produced the most. In all cases, the major carbon-containing products in the liquid phase were acetaldehyde, 2,3-butanediol and acetic acid. A relationship between the mean pore size and the yield of 2,3-butanediol was established with most being produced over Pt/A100 which had the smallest pore size.

1. Introduction

Great progress has been made in catalytic production of H_2 from renewable sources. The use of processes of thermal reforming of alcohols derived from biomass has been proposed as a mid-term solution to H_2 production but other more sustainable solutions are required for long-term applications [1–5]. One such possibility is water splitting over a semiconductor photocatalyst. For this purpose, one of the most studied semiconductors is TiO_2 [6,7]. The addition of noble metals to the TiO_2 decreases the hydrogen evolution overpotential and contributes to the suppression of recombination between the photogenerated holes (h^+) and photoinduced e^-. Most studies deal with TiO_2-based systems containing small amounts of Pt; although the addition of other noble metals such as Au or Pd, as well as the use of non-noble metals as co-catalysts has also been the object of numerous studies [6–9]. The work function of TiO_2 (4.2 eV) is lower than those of Pt, Pd and Au: 5.65, 5.55 and 5.10 eV, respectively. The Schottky barrier that can form at the metal/TiO_2 interface could decrease the rate of recombination of electron hole pairs; such an effect would be higher for metals with higher work functions and has been related to H_2 evolution [6]. The recombination rate of electron hole pairs could also be decreased by adding sacrificial reagents to the aqueous solution. Therefore, the use of aqueous solutions containing sacrificial organic reductants is currently a subject of interest in attempts to increase the extension of the total photocatalytic oxidation/reduction cycle [10,11]. During the photocatalytic process, the sacrificial substrates (electron donors) consume the photogenerated holes (h^+) and are consequently oxidized; while H^+ is reduced to H_2. One of the main roles of the sacrificial reductants is to speed up hole consumption thereby averting electron hole recombination [4,6]. Several oxygenate organic sacrificial reductants have been studied in this use, the most studied being methanol and ethanol [3–5,8–18]. Moreover, the use of biomass-derived alcohols could have several advantages in terms of sustainability; nowadays ethanol is produced from biomass worldwide and therefore ethanol can be considered an appropriate substrate for the process. When methanol or ethanol is used, they can be oxidized to formaldehyde or acetaldehyde respectively in a first step; then the corresponding aldehyde can itself act as a sacrificial agent and further

* Corresponding author at: Departament de Química Inorgànica i Orgànica, secció de Química Inorgànica and Institut de Nanociència i Nanotecnologia, Universitat de Barcelona, C/ Martí i Franquès 1-11, 08028, Barcelona, Spain.
E-mail address: narcis.homs@qi.ub.edu (N. Homs).

https://doi.org/10.1016/j.cattod.2018.06.017
Received 22 December 2017; Received in revised form 20 April 2018; Accepted 6 June 2018

oxidation can take place [16]. Although the main goal of such processes is H_2 production, the simultaneous valorisation of the initial alcohol through the production of other useful compounds is an important aspect, which has frequently been disregarded, and merits further research. Several studies have reported the production of C_{2n} diol by C−C bond formation using Pt/TiO_2 as a catalyst and the corresponding C_nOH as the sacrificial reagent [16,17,19–21]. For the production of 2,3-butanediol using ethanol as a sacrificial reagent, the formation of α-hydroxyethyl radicals ($\cdot CH(OH)CH_3$) from the reaction of ethanol with the hole followed by the coupling of two such radicals in solution has been proposed [21]:

$$CH_3CH_2OH + h^+ \rightarrow \cdot CH(OH)CH_3 + H^+ \quad (1)$$

$$2 \cdot CH(OH)CH_3 \rightarrow CH_3CH(OH)CH(OH)CH_3 \quad (2)$$

One could propose that an appropriate porous structure of the photocatalyst could favour the coupling of two $\cdot CH(OH)CH_3$ intermediate radicals (2) with respect to their oxidation:

$$\cdot CH(OH)CH_3 + h^+ \rightarrow CH_3CHO + H^+ \quad (3)$$

This led us to study the influence of the structural and morphological characteristics of porous Pt/TiO_2 on their photocatalytic ethanol-reforming behaviour. For this purpose, tailored Pt/TiO_2 catalysts with similar characteristics of the Pt metallic function and different structural and morphological characteristics were studied. Taking into account the fact that rutile TiO_2 is less active in water splitting than anatase TiO_2 is [7], different tailored Pt/TiO_2 catalysts containing only anatase (Pt/A50, Pt/A80 and Pt/A100) or both anatase and rutile (Pt/AR50, Pt/AR50-B and Pt/AR100) were prepared. Catalysts had similar Pt loading, and Pt dispersion. The smaller area and larger pore size of Pt/A50, Pt/AR50 and Pt/AR50-B compared to those of Pt/A80, Pt/A100 and Pt/AR100 allowed us to study textural effects of catalysts on the photocatalytic reaction. The catalytic behaviour of all the samples in terms of H_2 production and the valuable liquid byproducts yielded, including 2,3-butanediol, was analysed as a function of their characteristics. To this end, the catalysts were characterized using different physical-chemical techniques and, after the photocatalytic reaction, several post-reaction catalysts subjected to temperature programmed desorption (TPD) and oxidation (TPO) processes followed by diffuse reflectance infrared Fourier transform spectroscopy (DRIFTS), coupled with mass spectrometry (MS) analysis.

2. Experimental

2.1. Preparation of photocatalysts

Pt/TiO_2 photocatalysts (ca. 0.5% wt/wt.) were prepared by incipient wetness impregnation using $H_2PtCl_6{\cdot}6H_2O$ aqueous solutions and six porous TiO_2 with different morphological and structural characteristics. Three of the TiO_2 were commercial: Aeroxide P25 from Degussa, Anatase TiO_2 from Sigma Aldrich and TiO_2 from Tecnan: denoted as AR50, A50 and AR100, respectively. The TiO_2 AR50-B was prepared by treatment of AR100 at 873 K for 6 h in air. A80 and A100 were prepared by the evaporation-induced self-assembly (EISA) method using $Ti(OPr)_4$:HCl:H_2O:surfactant:decanol and $Ti(OPr)_4$:HCl:H_2O:surfactant:ethanol mixtures, respectively, to allow control of surface area and pore size [22]. An alcoholic solution of Sorbitane monostearate surfactant (Span® 60 from Sigma) was added to an acidified (HCl_{aq}) $Ti(OPr)_4$ solution and stirred for 5 h. The mixture was evaporated at 343 K and calcined at 473 K (2 h) and 673 K (12 h). In all cases, after Pt impregnation, the catalysts were dried at 343 K and then calcined at 673 K for 4 h.

2.2. Catalyst characterization

The Pt content of catalysts and that of solutions after the photocatalytic tests were determined by inductively-coupled plasma (ICP) atomic emission spectrometry using a Perkin Elmer Optima 3200RL equipment.

The surface area (S_{BET}), pore volume (V_{pore}) and pore diameters (D_{pore}) of the materials were determined by using N_2 adsorption-desorption isotherms at 77 K with a Micromeritics TriStar II 3020 apparatus.

X-ray diffraction (XRD) analysis used an Xpert PRO-diffractometer equipped with a CuKα radiation source (λ = 1.5406 Å) and a graphite monochromator. XRD patterns were collected between 2θ = 20° and 2θ = 100°, with a step width of 0.05° counting 3 s at each step. The mean TiO_2 crystallite size was estimated using the Scherrer equation: $D = k{\cdot}\lambda / \beta_{2\theta}{\cdot}\cos\theta_{max}$, where k is a constant which depends on the morphology of the crystalline phases present (k = 1), λ is the X-ray wavelength, $\beta_{2\theta}$ is the width at half height of an intense diffraction peak of the phase whose mean size is being determined: (101) and (110) for anatase and rutile respectively, and θ_{max} is the Bragg angle at the maximum of the peak.

Raman spectroscopy was performed using a Jobin-Yvon LabRam HR 800 in micro-Raman mode equipped with a CCD detector coupled to an Olympus BXFM optical microscope and using a 532 nm solid state laser (visible-Raman). Spectra were acquired using 3 accumulations of 5 s each. The samples were studied at 50x magnification. Laser power was limited to 1.5 mW.

UV-Visible diffuse reflectance spectra (UV–vis DRS) were collected using a Perkin Elmer Lambda 950 UV/Vis Spectrometer with a 3 nm slit width and a speed of 654.92 nm·min^{-1}. $BaSO_4$ was used as the reference. The reflectance spectra were analysed using the Kubelka-Munk formalism. Band-gap values were calculated using the Tauc plot $(F(R_\infty){\cdot}h\upsilon)^n$ versus hυ, where n = 1/2 denotes an indirect allowed transition [23].

Temperature programmed reduction (H_2-TPR) and CO chemisorption experiments were carried out using a Micromeritics Autochem II 2920 system. The sample (approximately 50 mg) was placed in a U-shaped quartz reactor and the reduction profile was obtained using a 10% (v/v) H_2/Ar flow, increasing the temperature from 253 K to 973 K at 10 K·min^{-1}. The amount of hydrogen consumed was determined using a thermal conductivity detector (TCD). For the CO chemisorption experiments, samples were previously reduced at 398 K with a 10% (v/v) H_2/Ar stream for 45 min, and then purged with He for 30 min at the same temperature; CO chemisorption was carried out at 308 K.

X-ray photoelectron spectroscopy (XPS) were collected with a Perkin Elmer PHI-5500 spectrometer equipped with an Al Kα source (1486.6 eV) and a hemispherical analyser. The pressure in the analysis chamber was maintained below 10^{-8} torr during data acquisition. Binding energy values were referenced to the adventitious C 1s peak at 284.8 eV.

High-resolution transmission electron microscopy (TEM) images were obtained using a JEOL JEM-2100 electron microscope working with an electron acceleration potential of 300 kV. The samples were deposited on copper grids from ethanol dispersions.

For the DRIFTS-MS studies, a Harrick Scientific HVC-DRP-4 DRIFTS cell attached to a Bruker VERTEX 70 FTIR spectrometer was coupled with a ThermoStar GSD320T1 mass spectrometer to analyse the gas evolved during the TPD and TPO treatments; a resolution of 2 cm^{-1} was used in the collection of spectra.

2.3. Photocatalytic measurements

Photocatalytic experiments were carried out in a glass reactor described elsewhere [16,17]. A broad-spectrum Hg lamp (Ace-Hanovia, maximum power at λ = 366 nm, 25.6 W (emission spectrum shown in Fig. S1, in Supporting information), was used. The lamp was placed in a quartz jacket cooled by water giving a light power radiation of 0.49 W/cm^2, and this ensemble plunged into the aqueous ethanol solution. The temperature of the reaction was maintained at 298 K. 0.5 g of catalyst and 0.250 L of (25% v/v) aqueous ethanol solution were used in all

cases.

Before each catalytic test, the suspension was flushed with a 40% (v/v) N_2/Ar mixture (24 mL·min^{-1}) for 30 min. In order to allow the stabilization of the system, the t = 0 of the photocatalytic test was considered after 10 min of lighting the lamp. The N_2/Ar flow was kept during the photocatalytic test; N_2 was used as internal standard for quantification of gaseous products evolved during the reaction. The reactor outlet was provided with a condenser, kept at 258 K, allowing the liquid products to continuously condense in the reactor. The gaseous outlet flow was periodically measured and on-line analysed by a Varian CP-4900 two channel gas micro-chromatograph equipped with M5 A BF 10 m and PPQ BF 10 m columns and TCD detectors. For samples containing Pt, a considerable increase of the outflow was noted after initial lighting due to the formation of gaseous products. At the end of the photocatalytic test, the liquid phase was analysed using a Bruker 450-GC gas chromatograph equipped with a CP-Sil 8 CB 30 m x 0.25 mm CP5860 and WAX columns and flame ionization and MS detectors. The ethanol concentration in the final solution was determined by IR-ATR spectroscopy using a Bruker Alpha FT-IR spectrometer and appropriate calibration solutions.

The apparent quantum yield of hydrogen (ϕ_{H_2}) was calculated with respect the number of electrons used in the hydrogen generation.

$$\phi H_2(\%) = \left(\frac{\text{number of reacted electrons}}{\text{number of incident photons}}\right) \times 100$$

$$= \left(\frac{\text{number of evolved } H_2 \text{ molecules} \times 2}{\text{number of incident photons}}\right) \times 100$$

The number of incident photons capable to generate a couple e^-/h^+ (1.69×10^{20} photons·s^{-1}) was estimated using the radiated watt density at the exterior wall surface of the quartz lamp jacket of all the spectral lines having enough energy (2.85 eV, $\lambda < 436$ nm) to generate a couple e-/h^+. More than the half of the total number of incident photons capable to generate a couple e-/h^+ (1.09×10^{20} photons·s^{-1}) had an energy higher than 3.39 eV ($\lambda < 366$ nm) (ACE GLASS photoelectric instrument company data).

3. Results and discussion

3.1. Characterization

As stated in the experimental section, Pt/A50, Pt/AR50, Pt/AR50-B, Pt/A80, Pt/A100 and Pt/AR100 catalysts were prepared; their main characteristics are shown in Table 1. The XRD patterns of Pt/A50, Pt/A80 and Pt/A100 only showed diffraction peaks characteristics of the anatase (JCPDS 00-021-1272) phase (Fig. 1). In accordance with the XRD results, the visible Raman spectra of Pt/A50, Pt/A80 and Pt/A100 (Fig. S2, in Supporting information), showed bands attributed solely to the presence of anatase at 142 cm^{-1} (E_g), 197 cm^{-1} (E_g), 399 cm^{-1} (B_{1g}), 514 cm^{-1} ($A_{1g}+B_{1g}$) and 639 cm^{-1} (E_g) [24]. On the other hand, the XRD patterns of Pt/AR50, Pt/AR50-B and Pt/AR100 showed, in addition to the peaks characteristic of anatase, other peaks of lower intensity corresponding to the presence of the rutile (JCPDS 01-076-0317) phase (Fig. 1). The amount of rutile (% wt/wt) in Pt/AR catalysts was estimated from the areas of the rutile (110) and the anatase (101) peaks, following the method described in [25]; it was in the range 22%–30% rutile wt/wt (Table 1). Apart from the Raman bands due to the anatase phase described above, visible-Raman spectra of Pt/AR50, Pt/AR50-B and Pt/AR100 (Fig. S2), showed a band of low intensity at 444 cm^{-1} which is assigned to the E_g mode of rutile. Furthermore, the band with a maximum at 637 cm^{-1} in the Raman spectra of Pt/AR50, Pt/AR50-B and Pt/AR100 was asymmetric due to the contribution of a component at approximately 610 cm^{-1} which is assigned to the A_{1g} mode of rutile [24]. Although the B_{1g} mode is also Raman active for rutile, the intensity of the corresponding band at 144 cm^{-1} is low and it overlaps with the most intense band of the anatase phase (the E_g mode).

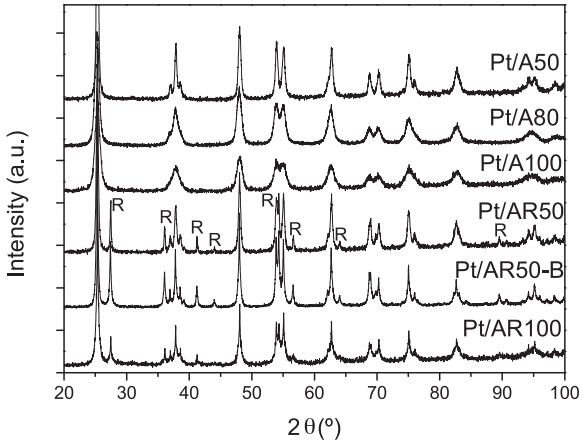

Fig. 1. XRD patterns of calcined catalysts. The peaks in the patterns of Pt/A50, Pt/A80 and Pt/A100 correspond to anatase; characteristic peaks of rutile (R) are indicated.

Table 1 also shows the crystallite sizes of the rutile and anatase phases in the catalysts estimated using the Scherrer equation. Catalysts containing only anatase, Pt/A50, Pt/A80 and Pt/A100, showed smaller crystallite sizes than those containing both anatase and rutile, Pt/AR50, Pt/AR50-B and Pt/AR100. Moreover, for catalysts containing both, anatase and rutile phases, the crystallite size of the rutile was always larger than that of the anatase; this agrees with the transformation sequence of the TiO_2 polymorphs, which is size dependent [25]. Table 1 shows the characteristics of the visible-Raman E_g band, the full width at half maximum (FWHM) and the Raman shift corresponding to the maximum, for catalysts which showed only visible-Raman bands characteristic of the anatase phase. Pt/A50 catalyst with larger crystallites than Pt/A80 and Pt/A100, showed a lower FWHM of the E_g band and a lower Raman shift. This is in agreement with previous work [26].

Fig. 2 shows the adsorption-desorption N_2-isotherms and the pore size distribution for most of catalysts; the corresponding pore volume appears in Table 1. For all catalysts, type IV(a) isotherms were found in

Table 1
Several characteristics of calcined Pt/TiO_2 catalysts. Anatase/rutile ratio (%, wt/wt) and crystallite size (D) of anatase (A) and rutile (R) were determined from XRD patterns. BET surface-area, pore volume (V_{pore}) and average pore diameter (D_{pore}), were determined from N_2 physisorption.

Catalyst	Anatase / Rutile (%, wt/wt)	D (nm) A/R	Anatase E_g vis-Raman band FWHM/position(cm^{-1})	Band-gap (eV)	S_{BET} (m^2·g^{-1})	V_{pore} (cm^3·g^{-1})	D_{pore} (nm)	Pt (%, wt/wt)
Pt/A50	100/0	22/-	11.96/142.5	3.18	51	0.31	29.1	0.56
Pt/A80	100/0	11/-	18.90/144.1	3.02	86	0.17	7.0	0.47
Pt/A100	100/0	9/-	16.06/144.0	3.16	96	0.14	4.7	0.37
Pt/AR50	70/30	26/49	–	2.92	48	0.31	42.7	0.50
Pt/AR50-B	76/24	47/52	–	2.93	50	0.34	30.4	0.55
Pt/AR100	78/22	43/62	–	2.89	102	0.23	12.7	0.54

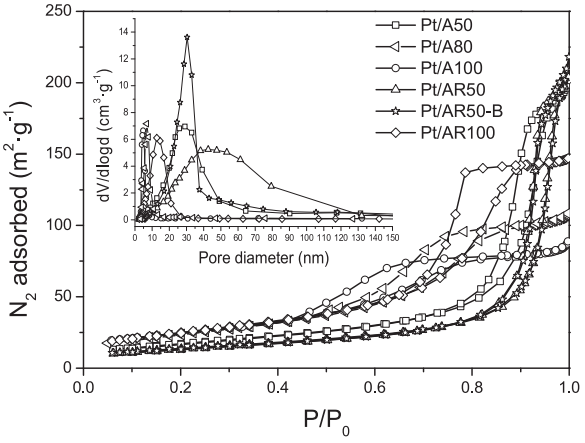

Fig. 2. Adsorption-desorption N_2-isotherms at 77 K and pore size distribution of calcined catalysts.

accordance with the new IUPAC classification [27]; the hysteresis loop was associated with capillary condensation in mesopores. Pt/A50, Pt/AR50 and Pt/AR50-B showed a similar shape of the loop, which corresponded to an H1 hysteresis loop. The shape of the hysteresis loop for Pt/A80, Pt/A100 and Pt/AR100 corresponded to the H2 type [27]. Pt/A80, Pt/A100 and Pt/AR100 showed a lower pore volume and pore size, and a narrower pore size distribution than Pt/A50, Pt/AR50, and Pt/AR50-B. Moreover, Pt/A80, Pt/A100 and Pt/AR100 showed a narrower pore size distribution than Pt/A50, Pt/AR50-B and Pt/AR50, being the latter the one that showed the widest range of pore size in the mesopore-macropore zone, in accordance with the characteristics already reported for the commercial AR50 support [28,29].

As stated in the experimental section, the UV–vis DR spectra were analysed using the Kubelka-Munk formalism (Fig. S3 in Supporting Information) and the band-gap values were determined (Table 1). The band-gap values of Pt/A catalysts were slightly higher than those of Pt/AR catalysts (Table 1). This accords with the higher band-gap value expected for pure anatase (3.20 eV) than that expected for pure rutile (3.00 eV) [7,14].

The calcined catalysts were also analysed by XPS; Ti 2p, O 1s, C 1s, Pt 4f core level spectra were recorded (Fig. S4 A–D in Supporting information). For all the catalysts, maxima of Ti 2p peaks at 458.6–458.8 eV (Ti $2p_{3/2}$) and 464.4–464.5 eV (Ti $2p_{1/2}$) were observed (Fig. S3 A). However, the spectrum corresponding to Pt/A100 clearly differs from the other spectra; the deconvolution of the Ti $2p_{3/2}$ peak reveals a component at 457.2 eV which could be formally assigned to the presence of surface Ti^{3+} species [30,31]. The O 1s level of the fresh catalysts showed maxima at 529.9–530.1 eV (Fig. S3 B). In all cases, O 1s peak deconvolution indicated the presence of a low-intensity component at 531.3 eV which is assigned to −OH surface groups. The components at lower BE are related to surface oxide ions [31]. The O 1s spectrum of Pt/A100 also differs from the others; from its deconvolution, a component at 528.5 eV is found, which could be related to surface oxide ions interacting with Ti^{3+} species. As stated in the experimental section, A100 was synthesized in the laboratory by EISA method using $Ti(OPr)_4$ and Span 60® as the surfactant. After calcination at 673 K, the solid obtained was not totally white but looked blue-greyish; this could be related to the presence of defective surface V_o-Ti^{3+} sites. On the other hand, no significant differences were observed in the C 1s spectra of the catalysts (Fig. S4 C). In all cases, the maximum of the corresponding Pt $4f_{7/2}$ component (Fig. S4 D) was located in the range 72.5–72.8 eV, indicating the presence of oxidized surface platinum species.

The Pt/Ti atomic ratios determined by XPS are compared to those determined by chemical analysis (CA) in Table 2. As expected, in all cases $(Pt/Ti)_{XPS}$ was higher than $(Pt/Ti)_{CA}$, indicating a segregation of

Table 2
Several characteristics of catalysts obtained from TPR experiments (H_2 consumption/Pt), CO chemisorption (Pt dispersion and Pt particle size), XPS (Pt/Ti atomic ratios) and mean turnover frequency (TOF).

Catalyst	H_2/Pt mol/mol	Pt dispersion (%)	Pt (nm)	$(Pt/Ti)_{XPS}$ atomic ratio		TOF (s^{-1})
				Calcined[a]	Post-reaction	$H_2/Pt_{surface}$ mol/mol
Pt/A50	1.72	52	2.2	0.0111 (0.0023)	0.0040	0.96
Pt/A80	2.35	56	2.0	0.0096 (0.0019)	0.0047	0.58
Pt/A100	1.73	49	2.3	0.0060 (0.0015)	0.0020	0.63
Pt/AR50	1.61	53	2.1	0.0101 (0.0021)	0.0040	0.66
Pt/AR50-B	0.58	56	2.0	0.0122 (0.0023)	0.0069	0.83
Pt/AR100	1.62	44	2.6	0.0070 (0.0022)	0.0030	0.48

[a] values into brackets refer to Pt/Ti atomic ratios determined by CA.

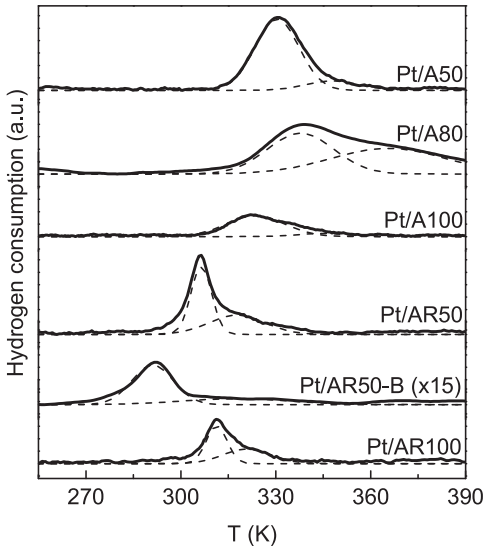

Fig. 3. TPR profiles of calcined catalysts.

Pt on the surface of the catalysts.

Reduction properties of the catalysts were determined by H_2-TPR experiments; the TPR profiles are shown in Fig. 3. Pt/A50, Pt/A80 and Pt/A100, which only contained anatase as the crystalline TiO_2 phase showed broad reduction peaks and slightly higher reduction temperatures than Pt/AR50, PtAR50-B and Pt/AR100, which contained both anatase and rutile. That could indicate that Pt species interact more strongly with the anatase phase than with the rutile phase. The TPR profiles corresponding to Pt/AR50, Pt/AR50-B and Pt/AR100 were asymmetric; they showed a maximum of hydrogen consumption at 291–313 K and then a shoulder at higher temperatures. The comparison of the TPR patterns in Fig. 3 could indicate that the H_2 consumption at 291–313 K found in the H_2-TPR profiles of Pt/AR50, Pt/AR50-B and Pt/AR100 might be related to the reduction of Pt species interacting with the rutile phase. Except for Pt/A80, the amount of H_2 consumed (Table 2) was lower than that necessary for reducing the nominal PtO_2 in the catalysts; this is probably due to a partial decomposition of PtO_2 during the calcination step, giving PtO and/or Pt° [32]. On the other hand, the high value of H_2 consumption determined for Pt/A80 catalyst could point to a partial reduction of the support probably due to a strong interaction of the Pt phases with the anatase phase. This catalyst showed an asymmetric H_2 consumption peak centred at 340 K with a

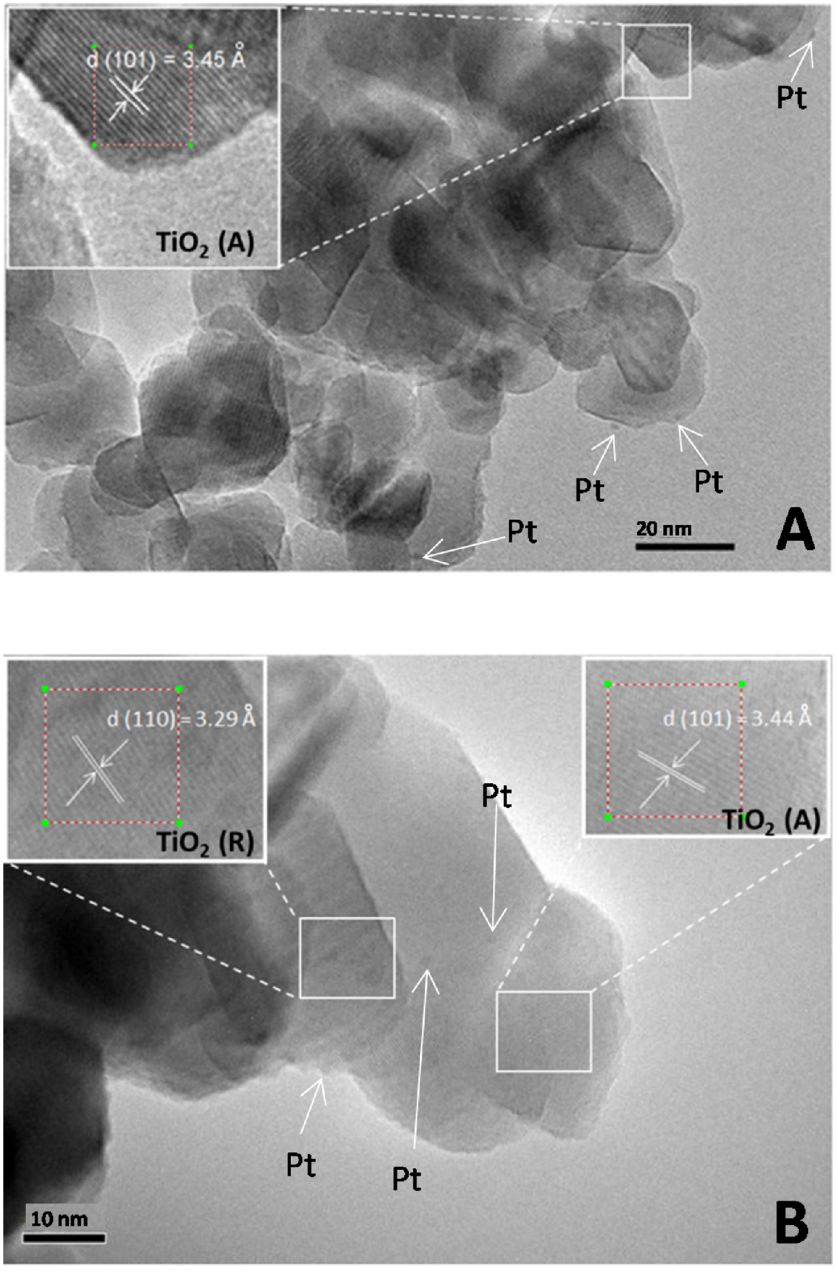

Fig. 4. TEM micrographs of reduced catalysts: A) Pt/A50; B) Pt/AR50.

prominent shoulder; its deconvoluted profile shows a component at 367 K (Fig. 3).

In order to compare the Pt dispersion of the catalysts, calcined catalysts were reduced at 398 K and then CO chemisorption was determined at 308 K. For the calculation of Pt dispersion, a stoichiometry of CO adsorption CO/surface Pt = 1 was assumed. Table 2 shows the metallic dispersion values that were in the range of 44%–56%. Assuming a cubic shape of the Pt particles, their mean size was calculated to be in the range 2.0–2.6 nm (Table 2). The presence of rather highly dispersed Pt was confirmed from the TEM analysis. Fig. 4 shows representative TEM micrographs of reduced Pt/A50 (Fig. 4A) and Pt/AR50 (Fig. 4B) catalysts. The analysis of the micrographs in Fig. 4A and B shows the presence of metallic particles that are homogeneous in size (about 2 nm), according to the Pt° particle size determined by CO chemisorption. High resolution images of some of TiO_2 particles indicated the presence of the anatase phase in Pt/A50 (Fig. 4A); and both anatase and rutile phases in Pt/AR50 (Fig. 4B), in agreement with the XRD and Raman results.

It is worth mentioning that Pt/A50, Pt/AR50 and Pt/AR50-B, which show similar values of BET surface-area, Pt content and Pt particle size determined from CO chemisorption, also showed similar $(Pt/Ti)_{XPS}$ ratios (Table 2). This supports the dispersion values determined by CO chemisorption and allows for appropriate comparison of the catalytic behaviour of Pt/A50, Pt/AR50 and Pt/AR50-B as a function of their structural and morphological characteristics.

3.2. Photocatalytic behaviour

As stated above, the photocatalytic behaviour of all the samples was tested for 4 h at 298 K using 25% v/v aqueous ethanol solutions and the gas evolved from the reactor was periodically sampled and analysed.

Fig. 5A shows the total amount of evolved H_2 as a function of irradiation time for Pt/TiO_2 catalysts and the corresponding supports. The Pt-containing catalysts produced much more H_2 than the TiO_2

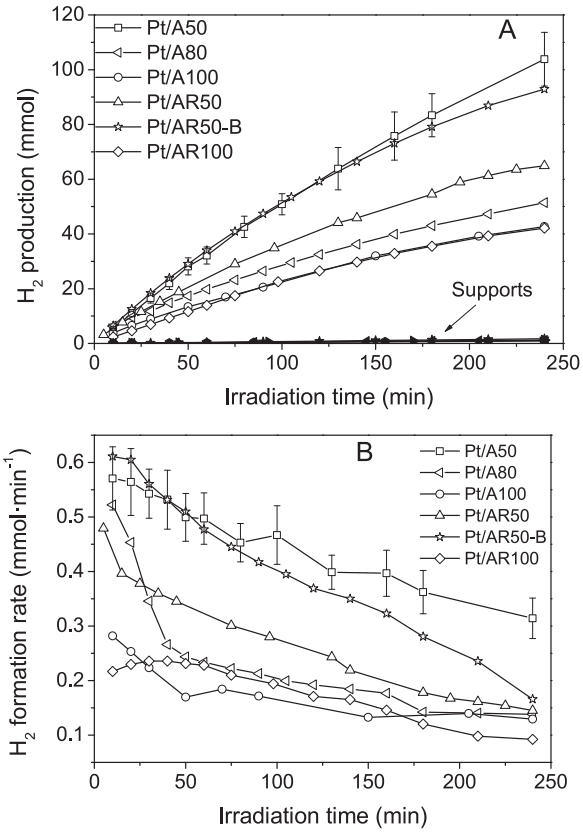

Fig. 5. H_2 produced from aqueous solutions of ethanol 25% v/v as a function of the irradiation time over several Pt/TiO_2 catalysts and the corresponding TiO_2: A) total amount of H_2; B) rate of H_2 production. The deviation bars are generated from the variation on the H_2 produced in four separate experiments carried out over the Pt/A50 catalyst.

supports, which showed negligible photocatalytic activity under the experimental conditions used. There is an accepted difficulty in the quantitative comparison of the amount of hydrogen produced by different catalysts if different photocatalytic reactors with different geometries and excitation sources with different intensities and wavelengths are used for carrying out the photocatalytic test [33]. Although for solving this problem the use of the hydrogen apparent quantum yield (ϕ_{H_2}) has been proposed, the dependence of the ϕ_{H_2} on the excitation wavelength could hinder a straightforward comparison if an excitation source with multiple irradiation lines is used. For Pt/TiO_2 nanotubes, a clear dependence of the ϕ_{H_2} on the excitation wavelength has been shown; higher ϕ_{H_2} were obtained when sources of irradiation with λ lower than 365 nm were used compared to ϕ_{H_2} obtained with a λ of 365 nm irradiation (ϕ_{H_2} of 1% and 16% were found for irradiation sources of 365 nm and 313 nm respectively for methanol/water mixtures) [33]. This effect has been related with the excess of photon energy with respect the TiO_2 band-gap energy [33]. As stated in the experimental section, in this work a lamp providing different irradiation lines was used. The total number of incident photons with energy higher than 2.85 eV was estimated to be 1.69×10^{20} photons·s^{-1} and more than a half of this total number (1.09×10^{20} photons·s^{-1}) had energy $\geq$ 3.39 eV. It has been proposed that the use of photons with an excess of energy with respect the TiO_2 band gap energy could increase the life-time of electrons and holes and then they could reach the surface more easily and increase the ϕ_{H_2} [33]. From the values of total hydrogen production in Fig. 5A and the total number of incident photons of more than 2.85 eV, the ϕ_{H_2} values for the catalysts were calculated: Pt/A50, 5.14% > Pt/AR50-B, 4.73% > Pt/AR50, 3.22% > Pt/A80, 2.81% > Pt/A100, 2.11% > Pt/AR100, 2.08%. The same trend followed the total amount of H_2 produced relative to the Pt content of the catalysts.

Samples with a surface area of approximately 50 $m^2 \cdot g^{-1}$ and a larger pore size, performed better than those with a larger surface area (80-100 $m^2 \cdot g^{-1}$) and a smaller pore size. Although for the Pt/TiO_2 catalysts, H_2 is produced continuously during the catalytic test, the rate of H_2 production decreased in all cases with increasing irradiation time; the rate of H_2 production and its decrease depended on the catalyst (Fig. 5B). Pt/A50, which contained only anatase as the crystalline phase of TiO_2, not only produced the most H_2 but it showed the lowest deactivation during the reaction time.

As an attempt to rationalize the hydrogen production as a function of the intrinsic characteristics of the catalysts, we calculated the amount of H_2 produced (mol) per second and by surface amount of Pt (mol) (mean turnover frequency (TOF)). In this way, the catalytic results are relative to exposed Pt sites for H^+ reduction. As stated above, for each catalyst, the amount of surface Pt was estimated, after H_2-reduction at 398 K, from the CO chemisorption experiments; and the TOF values determined were used for comparative purposes. TOF values are compiled in Table 2 and followed the trend: Pt/A50 > Pt/AR50-B > Pt/AR50 > Pt/A100 > Pt/A80 > Pt/AR100. In this respect, it should be noted that although Pt/A50 and Pt/AR50 and Pt/AR50-B have similar values of BET surface area, Pt content and dispersion, the performance of Pt/A50 was better than that of Pt/AR50 and Pt/AR50-B in terms of both H_2 production and stability (Fig. 5). The structural characteristics of TiO_2 and/or the porous distribution could play a decisive role in the photocatalytic behaviour of these samples. As stated above, TPR experiments indicate that Pt species interact more strongly with TiO_2 in Pt/A50 than in Pt/AR50. This could improve the charge separation in Pt/A50 with respect Pt/AR50 and consequently it could reduce electron/hole recombination in the former.

In all cases, H_2 was the major gas product formed during reaction, although other carbon-containing products such as CO, CO_2, CH_4, C_2H_4 and C_2H_6 were also determined in the gas phase. For all the catalysts, the amount of CO, CO_2, CH_4, C_2H_4 and C_2H_6 found was very small compared to the amount of H_2 evolved (Table 3). After 4 h of reaction, the H_2/CO_x molar ratio was in the range 18–36, which indicates that in all cases the reforming of ethanol is a minority process with the formation of intermediate products being favoured. The analysis of the liquid phase after the photocatalytic reaction allowed us to determine

Table 3
Total amount of gaseous products and, acetaldehyde, acetic acid and 2,3-butanediol obtained from the photocatalytic reaction of ethanol aqueous solutions (25% v/v) over the different Pt/TiO_2 catalysts (0.5 g) after 4 h of irradiation at 298 K.

	Total amount (mmol)								
Catalyst	H_2	CO_2	CO	CH_4	C_2H_4	C_2H_6	CH_3CHO	CH_3COOH	2,3-butanediol
Pt/A50	103.8	4.1	0.7	4.9	0.0	0.9	101.4	3.8	8.5
Pt/A80	56.8	0.7	0.9	1.1	0.0	0.5	51.8	2.6	26.1
Pt/A100	42.7	0.6	0.8	1.1	0.1	0.6	34.7	1.0	30.1
Pt/AR50	64.9	2.3	1.3	3.0	0.0	0.6	85.7	2.8	7.9
Pt/AR50-B	95.4	2.3	1.2	2.3	0.1	0.4	n.d.	3.4	6.2
Pt/AR100	42.1	0.7	0.6	0.9	0.0	0.2	n.d.	0.7	12.0

the ethanol conversion that was in the range 6.3%–17.3%. Besides ethanol and acetaldehyde, 2,3-butanediol, acetic acid, and small amounts of other heavier condensation products were identified in the liquid phase. The formation of these liquids products has been discussed previously [16].

Acetaldehyde is formed by ethanol dehydrogenation:

$$CH_3CH_2OH \rightarrow CH_3CHO + H_2 \quad (4)$$

Once acetaldehyde is formed, it can be oxidized to CH_3COOH:

$$CH_3CHO + H_2O \rightarrow CH_3COOH + H_2 \quad (5)$$

However, the Cannizaro disproportionation cannot be ruled out:

$$2CH_3CHO + H_2O \rightarrow CH_3CH_2OH + CH_3COOH \quad (6)$$

CO, CO_2 and CH_4 can be formed from CH_3CHO and/or CH_3COOH decomposition:

$$CH_3CHO \rightarrow CH_4 + CO \quad (7)$$

$$CH_3COOH \rightarrow CH_4 + CO_2 \quad (8)$$

Meanwhile, the reforming of acetaldehyde and acetic acid can produce CO_2 and H_2:

$$CH_3CHO + 3H_2O \rightarrow 2CO_2 + 5H_2 \quad (9)$$

$$CH_3COOH + 2H_2O \rightarrow 2CO_2 + 4H_2 \quad (10)$$

Although in all cases the amounts of CH_3COOH and CO_2 were low compared to those of H_2 produced, in general they were slightly higher for catalysts with surface-area of approximately 50 m^2g^{-1} than for catalysts having higher surface-areas; this could be related to the greater extent of reaction (4) and the subsequent oxidation of acetaldehyde over the former catalysts. Fig. 6 shows the variation in the amount of 2,3-butanediol produced with respect to the mean pore size of the catalysts; the smaller the pores, the greater the 2,3-butanediol production. Over catalysts with smaller pore size (Pt/A80, Pt/A100 and Pt/AR100), the formation of 2,3-butanediol was favoured by the coupling of two α-hydroxyethyl radicals (2).

The Pt content of the post-photocatalytic reaction solutions was analysed and the amount of Pt found was always lower than 1% of the original Pt content in the catalysts; this pointed that the leaching of Pt was not the main cause of the deactivation of catalysts.

The catalysts were analysed by XPS after the photocatalytic reaction. In all post-reaction samples, the maxima of the Pt $4f_{7/2}$ located at 70.0–70.5 eV (Fig. S4 E) indicate the formation of Pt^0 during the photocatalytic test, which probably occurred at the initial irradiation period. Moreover, in all cases, the Pt/Ti ratios determined by XPS after

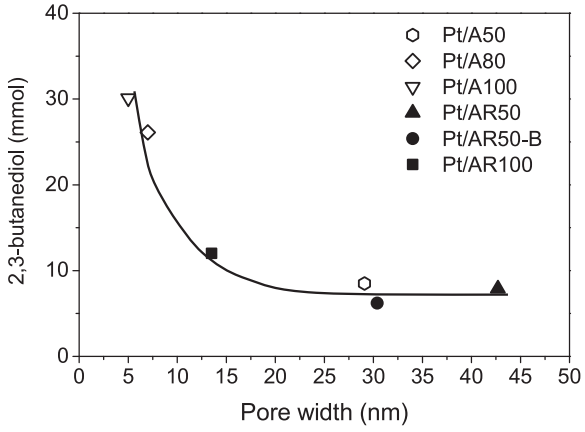

Fig. 6. 2,3-butanediol produced from the photocatalytic reaction of ethanol aqueous solution (25% v/v) as a function of the pore size of Pt/TiO_2 catalysts. Irradiation time 4 h, T = 298 K.

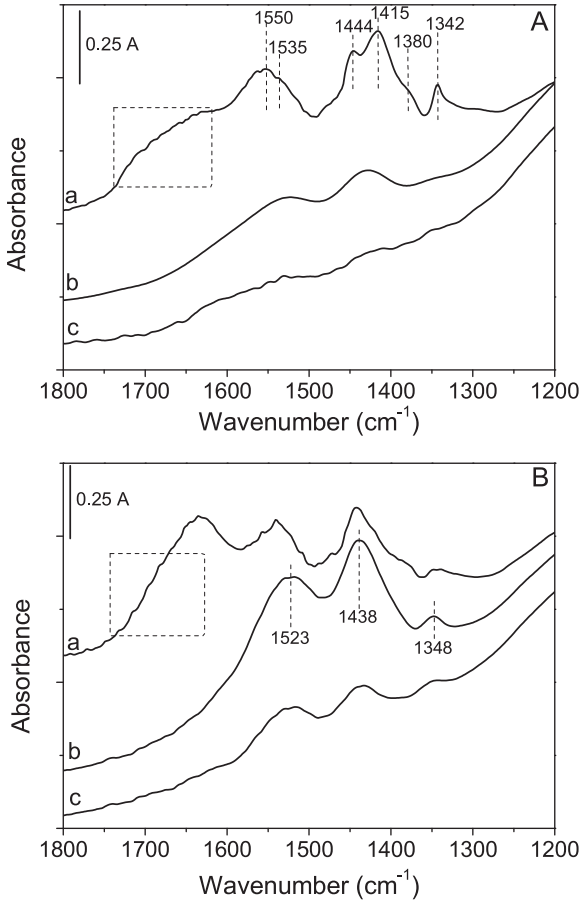

Fig. 7. DRIFT spectra of Pt/A50 (A) and Pt/AR50-B (B) post-reaction catalysts: (a) after reaction, catalyst was treated at 298 K under He flow; (b), after (a), temperature was increased up to 623 K under He flow; (c), after (b) catalyst was treated 30 min at 623 K under O_2/He flow.

the photocatalytic test were lower than those of the catalysts before the reaction (Table 2). This decrease in the Pt/Ti surface ratio could be related to the deactivation of the catalysts. However, it is necessary to recall that the photocatalytic reaction takes place in liquid phase and that the liquid products are not separated of the reaction media during the catalytic test; a competition between ethanol and some of the products for the catalysts adsorption sites has been proposed, this could contribute to the deactivation of catalysts [16].

For a better insight in the characteristics of the species adsorbed on the surface of the post-reaction catalysts, Pt/A50 and Pt/AR50-B were examined after reaction using DRIFTS and on-line MS analysis. After 4 h of photocatalytic reaction, Pt/A50 and Pt/AR50-B produced 103.8 mmol and 95.4 mmol of H_2, respectively (Table 3). Pt/A50 and Pt/AR50-B presented a similar initial rate of H_2 production; however, Pt/AR50-B showed a higher deactivation (Fig. 5B). In separate experiments, post-reaction Pt/A50 and Pt/AR50-B were treated under He flow from 298 K to 623 K (TPD) and then at 623 K under an O_2/He mixture (TPO). Fig. 7 shows the corresponding DRIFT spectra of Pt/A50 (after a 8 h catalytic test) (Fig. 7A) and Pt/AR50-B (after the standard catalytic test, 4 h) (Fig. 7B). Spectra a and b in Fig. 7 correspond to the initial post-reaction catalysts under He flow at 298 K (spectra a) and those after TPD up to 623 K (spectra b), respectively. Although the assignation of bands is not straightforward because several carboxylate and carbonate species show absorption bands in this zone, there are several spectral features that should be remarked. Initially, both post-reaction Pt/A50 and Pt/AR50-B showed bands of similar intensity, but after TPD up to 623 K, the intensity of those of Pt/A50 decreased in a great extension (spectrum b in Fig. 7A). On the contrary, after TPD up to 623 K,

intense bands remained for the Pt/AR50-B (spectrum b in Fig. 7B). Post-reaction Pt/A50 catalyst initially showed a broad absorption in the 1735-1650 cm^{-1} zone which could be assigned to υ(C═O) of aldehydic species, likely acetaldehyde, and/or acetic acid [16,17,34,35]. Moreover, from the spectrum a in Fig. 7A the presence of several carboxylate species over post-reaction Pt/A50 can be proposed. The wide bands in the zones 1590-1525 cm^{-1} and 1480-1360 cm^{-1} can be reasonably assigned to υ_{as}(COO) and υ_{s}(COO) of $CH_3COO^-_{ad}$ and $HCOO^-_{ad}$ species, and the band at 1342 cm^{-1} to $\delta_s(CH_3)$ of adsorbed CH_3COO^- [34]. During the TPD of post-reaction Pt/A50, besides the formation of CO_2 ($m/z = 44$), that of CO ($m/z = 28$) and CH_4 ($m/z = 16$) was determined by MS analysis of the outlet flow, that indicating an easy decomposition of adsorbed carboxylate and aldehydic species. On the contrary, although during the TPD of post-reaction Pt/AR50-B, CO_2 was formed, neither CO or CH_4 were detected, and high intensity bands centred at 1523 cm^{-1}, 1438 cm^{-1} and 1348 cm^{-1} remained after the TPD treatment at 623 K. The presence of different surface acetate species which could not be totally removed during the thermodesorption process can be proposed in this case [36]. A subsequent oxidation treatment at 623 K of both post-reaction catalysts, Pt/A50 and Pt/AR50-B, produced the main formation of CO_2, and H_2O. After this treatment, DRIFT spectra pointed to the almost total disappearance of surface species for both post-reaction Pt/A50 and Pt/AR50-B catalysts (spectra c in Fig. 7A and B).

The acetate species strongly bonded on the surface of Pt/AR50-B could contribute to its deactivation during the photocatalytic test. We have recently reported that, in vapour phase, the photodegradation of ethanol in the presence of water and O_2 was more effective over A50 TiO_2 than over AR50 TiO_2, on the later strongly bonded bidentate acetate species were formed [37]. However, other factors than the characteristics of TiO_2 could influence in the deactivation of catalysts, as the presence of chemisorbed species on Pt centres [16,17].

4. Conclusion

The structural and morphological characteristics of tailored Pt/TiO_2 determine the photocatalytic transformation of aqueous ethanol solutions in terms of H_2 and valuable by-products yielded.

Pt/A50, Pt/AR50 and Pt/AR50-B with lower surface area and higher pore size than Pt/A80, Pt/A100 and Pt/AR100, showed a better photocatalytic performance for hydrogen production. Pt/A50 (51 $m^2 \cdot g^{-1}$, mean pore size 29.1 nm), in which the presence of only anatase as the crystalline phase was determined, showed the highest total H_2 production (hydrogen apparent quantum yield, $\phi_{H_2} = 5.14\%$) and the lowest deactivation. Surface carboxylate species were found on post-reaction catalysts; for Pt/A50 these species were more easily removed than for Pt/AR50-B, which showed a higher deactivation than the former.

Acetaldehyde, 2,3-butanediol and acetic acid were the major products found in the liquid phase after the photocatalytic tests. A relationship between the yield of 2,3-butanediol and the pore size of catalysts was found. The lower the pore size, the higher the yield of 2,3-butanediol. Over Pt/A80 and Pt/A100, the coupling of two α-hydroxyethyl radicals was favoured and 2,3-butanediol was formed. Using Pt/A100 (96 $m^2 \cdot g^{-1}$, mean pore size 4.7 nm), the most 2,3-butanediol was obtained.

Acknowledgements

The authors are grateful to the Spanish MINECO-FEDER projects MAT2014-52416-P and MAT2017-87500-P for financial support. A. C. Sola thanks the IREC for his PhD grant. M. S. Suliman Mohamed and A. Bonilla are acknowledged for the preparation of Pt/A80 and A100 respectively.

Appendix A. Supplementary data

Supplementary material related to this article can be found, in the online version, at doi:https://doi.org/10.1016/j.cattod.2018.06.017.

References

[1] P. Ramírez de la Piscina, N. Homs, Chem. Soc. Rev. 37 (2008) 2459–2467.
[2] D.I. Kondarides, V.M. Daskalaki, A. Patsoura, X.E. Verykios, Catal. Lett. 122 (2008) 26–32.
[3] V. Dal Santo, A. Gallo, A. Naldoni, M. Guidotti, R. Psaro, Catal. Today 197 (2012) 190–205.
[4] M. Bowker, Green Chem. 13 (2011) 2235–2246.
[5] X. Chen, S. Shen, L. Guo, S.S. Mao, Chem. Rev. 110 (2010) 6503–6570.
[6] A.L. Linsebigler, J.T. Yates Jr., G. Lu, Chem. Rev. 95 (1995) 735–758.
[7] D.Y.C. Leung, X. Fu, C. Wang, M. Ni, M.K.H. Leung, X. Wang, X. Fu, ChemSusChem 3 (2010) 681–694.
[8] A.V. Puga, A. Forneli, H. García, A. Corma, Adv. Funct. Mater. 24 (2014) 241–248.
[9] M.V. Dozzi, G.L. Chiarello, M. Pedroni, S. Livraghi, E. Giamello, E. Selli, Appl. Catal. B Environ. 209 (2017) 417–428.
[10] G.N. Nomikos, P. Panagiotopoulou, D.I. Kondarides, X.E. Verykios, Appl. Catal. B Environ. 146 (2014) 249–257.
[11] E.P. Melián, M.N. Suárez, T. Jardiel, J. Doña Rodríguez, A.C. Caballero, J. Araña, D.G. Calatayud, O.G. Díaz, Appl. Catal. B Environ. 152–153 (2014) 192–201.
[12] M. Cargnello, A. Gasparotto, V. Gombac, T. Montini, D. Barreca, P. Fornasiero, Eur. J. Inorg. Chem. (2011) 4309–4323.
[13] M. Bowker, C. Morton, J. Kennedy, H. Bahruji, J. Greves, W. Jones, P.R. Davies, C. Brookes, P.P. Wells, N. Dimitratos, J. Catal. 310 (2014) 10–15.
[14] K. Shimura, H. Yoshida, Energy Environ. Sci. 4 (2011) 2467–2481.
[15] P. Panagiotopoulou, E.E. Karamerou, D.I. Kondarides, Catal. Today 209 (2013) 91–98.
[16] A.C. Sola, N. Homs, P. Ramírez de la Piscina, Int. J. Hydrogen Energy 41 (2016) 19629–19636.
[17] A.C. Sola, M. Broch Gösser, P. Ramírez de la Piscina, N. Homs, Catal. Today 287 (2017) 85–90.
[18] G.L. Chiarello, D. Ferri, E. Selli, J. Catal. 280 (2011) 168–177.
[19] H. Lu, B. Zhao, D. Zhang, Y. Lv, B. Shi, X. Shi, J. Wen, J. Yao, Z. Zhu, J. Photochem. Photobiol. A Chem. 272 (2013) 1–5.
[20] J. Wang, P. Yang, B. Cao, J. Zhao, Z. Zhu, Appl. Surf. Sci. 325 (2015) 86–90.
[21] H. Lu, J. Zhao, L. Li, L. Gong, J. Zheng, L. Zhang, Z. Wang, J. Zhang, Z. Zhu, Energy Environ. Sci. 4 (2011) 3384–3388.
[22] A.C. Sola, A. Bonilla, P. Ramírez de la Piscina, N. Homs, Louvain-la-Neuve, Belgium, 11th Int. Symp. Sci. Bases Prep. Heterog. Catal., Ku Leuven (2014) 329–330.
[23] D. Reyes-Coronado, G. Rodríguez-Gattorno, M.E. Espinosa-Pesqueira, C. Cab, R. de Coss, G. Oskam, Nanotechnology 19 (2008) 145605.
[24] J. Zhang, M. Li, Z. Feng, J. Chen, C. Li, J. Phys. Chem. B 110 (2006) 927–935.
[25] H. Zhang, J.F. Banfield, J. Phys. Chem. B 104 (2000) 3481–3487.
[26] S. Kelly, F.H. Pollak, M. Tomkiewicz, J. Phys. Chem. B 101 (1997) 2730–2734.
[27] M. Thommes, K. Kaneko, A.V. Neimark, J.P. Olivier, F. Rodriguez-Reinoso, J. Rouquerol, K.S.W. Sing, Pure Appl. Chem. 87 (2015) 1051–1069.
[28] M.C. Hidalgo, G. Colón, J.A. Navío, J. Photochem. Photobiol. A Chem. 148 (2002) 341–348.
[29] Y. Yan, J. Wang, W. Wang, J. Sun, D. Wang, Q. Li, M. Babikier, H. Wang, Q. Yu, S. Jiao, S. Gao, H. Li, Electrochim. Acta 114 (2013) 681–687.
[30] U. Diebold, Surf. Sci. Rep. 48 (2003) 53–229.
[31] G. Liu, J. Pan, L. Yin, J.T. Irvine, F. Li, J. Tan, P. Wormald, H.M. Cheng, Adv. Funct. Mater. 22 (2012) 3233–3238.
[32] L.K. Ono, J.R. Croy, H. Heinrich, B.R. Cuenya, J. Phys. Chem. C 115 (2011) 16856–16866.
[33] M.P. Languer, F.R. Scheffer, A.F. Feil, D.L. Baptista, P. Migowski, G.J. Machado, D.P. De Moraes, J. Dupont, S.R. Teixeira, D.E. Weibel, Int. J. Hydrogen Energy 38 (2013) 14440–14450.
[34] B. Hauchecorne, D. Terrens, S. Verbruggen, J.A. Martens, H. Van Langenhove, K. Demeestere, S. Lenaerts, Appl. Catal. B Environ. 106 (2011) 630–638.
[35] B.I. Stefanov, Z. Topalian, C.G. Granqvist, L. Österlund, J. Mol. Catal. A Chem. 381 (2014) 77–88.
[36] J.M. Coronado, S. Kataoka, I. Tejedor-Tejedor, M.A. Anderson, J. Catal. 219 (2003) 219–230.
[37] A.C. Sola, D. Garzón Sousa, J. Araña, O. González Díaz, J.M. Doña Rodriguez, P. Ramírez de la Piscina, N. Homs, Catal. Today 266 (2016) 53–61.